

The Cas A - like SNR 1E 0102.2-7219 in the SMC: An Asymmetric Bipolar Explosion

Frédéric Vogt^{1,2} and Michael A. Dopita¹

ABSTRACT

We have used the *Wide Field Spectrograph* (WiFeS) on the 2.3m telescope at Siding Spring Observatory to map the [O III] 5007Å dynamics of the young oxygen-rich supernova remnant 1E 0102.2-7219 in the Small Magellanic Cloud. From the resultant data cube, we have been able to reconstruct the full 3-D structure of the system of [O III] filaments. From this we are able to deduce that the ejecta trace an asymmetric bipolar structure. The red-shifted gas contains fainter clumps but with higher velocities than the blue-shifted gas. The major axis of the explosion is inclined at $\sim 40^\circ$ to the line of sight. This structure shows that the supernova explosion has been influenced both by the rotation of the progenitor star and, presumably, by a global rotational instability following core collapse.

Subject headings: galaxies: Magellanic Clouds– ISM: supernovae remnants, kinematics and dynamics, individual (1E 0102.2-7219) – techniques: radial velocities – shock waves

1. Introduction

In the majority of supernova remnants, the optical emission arises from radiative shocks propagating into the surrounding interstellar medium. In these objects the ejecta of the star has been fully thermalized by the reverse shock and can be traced only at X-ray wavelengths. However, there exists a rare class young core-collapse supernova remnants in which the

¹Mount Stromlo and Siding Spring Observatories,
Research School of Astronomy and Astrophysics,
Australian National University, Cotter Road,
Weston Creek, ACT 2611, Australia.

²Laboratoire d’Astrophysique,
Ecole Polytechnique Fédérale de Lausanne,
Observatoire de Sauverny, 1290 Versoix, Switzerland.

amount of circumstellar and interstellar gas swept up by the blast wave of the supernova explosion is appreciably less than the mass ejected in the explosion. In these objects, dense clouds of ejecta formed by thermal instability during the fireball stage are shocked, destroyed and thermalized as they pass through the reverse shock. The optical spectrum of these objects is characterized by the complete absence of hydrogen and helium recombination lines and very strong forbidden lines of the α -process elements; oxygen, neon and sometimes argon, sulfur and calcium, reflecting the chemical composition of the helium-burnt core of the parent star. Those objects are also referred to as oxygen-rich supernovae, as the [O II] and [O III] forbidden lines of oxygen are the strongest in their spectrum.

Since the lifetime of the oxygen-rich supernova remnant before the full thermalization of the ejecta is quite short, only a handful of such objects are known. Mostly these are found in the Galaxy and the Magellanic Clouds, and the full list is sufficiently short to be given here. The most famous is Cas A (Kirshner & Chevalier 1977; Chevalier & Kirshner 1978) for which detailed HST proper-motion data have recently been obtained (Fesen et al. 2006a,b). A second Galactic example is G292.0+1.8 (Goss et al. 1979; Murdin & Clark 1979). Oxygen-rich filaments have also been found in Puppis A (Winkler & Kirshner 1985). Two more oxygen-rich SNR are known in the Large Magellanic Cloud (LMC), N132D (Danziger & Dennefeld 1976) and 0540-69.3 (Mathewson et al. 1980), and one has been discovered in the Small Magellanic Cloud (SMC), 1E 0102.2-7219 (Dopita et al. 1981). Further away, we find the extraordinary SNR in NGC 4449 (Kirshner & Blair 1980). Finally, five candidates were found recently in M83 using the Wide Field Camera 3 on the *Hubble Space Telescope* (Dopita et al. 2010b).

Although it is clear that the optically-emitting filaments are excited by slow shocks driven through them as they penetrate the reverse shock associated with the blast wave, the exact physics of their excitation remains somewhat incomplete. The first attempt to model them was made by Itoh (1981) who showed that the shocked pure-oxygen plasma could cool to a few hundred degrees Kelvin before recombining. Subsequently, Dopita et al. (1984) extended this theory to gas compositions including other elements. A more complete theory was developed by Sutherland & Dopita (1995) who showed that the cloud interaction forms a bow shock and cloud shock structure. The photons generated in the radiative cloud shock drive a weak R-type ionization front ahead of it, and the optical spectrum is the result of the combined shock and ionization front emission. In this model, the oxygen-rich condensations remain visible only until the slow cloud shock has been driven through them. This would explain why the individual fast moving knots and filaments in Cas A seem to have a typical lifetime of only about 10 yrs (van den Bergh & Dodd 1970).

The shape of the reverse shock is not necessarily spherical. It can be shaped by a varying

distribution of the density of the surrounding medium, either due to a density gradient in the interstellar medium, or due to pre-supernova mass loss. In addition, any asymmetries imposed during the explosion will play a major role, by imposing a varying kinetic energy density of the ejecta. Such asymmetries would be caused by the combination of rotation and collapse of the parent star, or - if the SN was in a binary - the break up of the binary system. Thus the shape of the reverse shock holds important clues about the nature of the supernova event. Indeed, if jets form, then these may well be related to the γ -ray Burst (GRB) phenomenon in core collapse supernovae.

There is observational evidence that many of these phenomena occur in the real world. In the case of Cas A, there is clear evidence of jet formation at optical (Fesen et al. 2001, 2006a,b), X-ray (Vink 2004; Hwang et al. 2004; Laming et al. 2006), and at infrared wavelengths (Hines et al. 2004). Schure et al. (2008) have shown that this phenomenon can be explained if the precursor lost mass as a slow red-giant wind, followed by a much faster Wolf-Rayet phase of evolution. However, the relative lifetimes of these phenomena are rather tightly constrained by the observations (Schure et al. 2008; van Veelen et al. 2009).

In the case of G292.0+1.8, Lee et al. (2010) infer that the X-ray data imply that the SNR currently expanding within the medium with a stellar wind density profile, $\rho \propto r^{-2}$. This would have been produced by a slow RSG wind from the progenitor star with a mass-loss rate of $\dot{M} = (2 - 5) \times 10^{-5} M_{\odot} \text{ yr}^{-1}$. For Puppis A, Winkler & Petre (2007) finds that a neutron star with a very high transverse velocity ($\sim 1600 \text{ km s}^{-1}$) has been ejected from the explosion centre, while proper-motion measurements demonstrate that the system of the fast-moving oxygen-rich knots are moving in the opposite direction.

In this paper we discuss the dynamics of the oxygen-rich SNR in the SMC, 1E 0102.2-7219. This was first discovered as a bright *Einstein Observatory* X-ray source (Seward & Mitchell 1981), and its optical counterpart was discovered by Dopita et al. (1981). It consists of a system of bright [O III]-emitting filaments some 6.9 pc in diameter, surrounded by a diffuse high-excitation shell with an inner radius of about 11pc. Later *Chandra Observatory* X-ray data obtained by Gaetz et al. (2000) showed that the emission associated with the outer blast wave has a diameter similar to this diffuse shell, so presumably the diffuse emission is the local interstellar medium excited by the X-rays coming from the remnant. Within the blast wave is a bright irregular ring of X-ray emission coincident in size with the [O III] filaments, which traces the position of the reverse shock. The 4790- MHz *Australia Telescope Compact Array* radio image of 1E 0102.2-7219 obtained by Amy & Ball (1993) shows that the radio emission is broadly confined between the outer blast wave and the reverse shock.

Spectroscopy of 1E 0102.2-7219 was used to establish that the oxygen-emitting filaments have both high temperature and low density and appear to consist only of Oxygen and of

Neon (Dopita & Tuohy 1984). Lasker & Golimowski (1991) failed to find any trace of Sulfur emission with deeper spectra. Spectra were later obtained by Blair et al. (2000) in both the UV and at optical wavelengths using the *Faint Object Spectrograph* (FOS) of the *Hubble Space Telescope* (HST). The UV spectra revealed the presence of both Carbon and Magnesium. In the X-ray regime, a *Chandra* spectrum was obtained by Hughes et al. (2000). Using the ESA *XMM-Newton Observatory*, a low-resolution spectrum was obtained with the EPIC instrument by Sasaki et al. (2001) and a high resolution soft X-ray spectrum was obtained by Rasmussen et al. (2001) using the RGS instrument on the same spacecraft. Flanagan et al. (2004) also obtained an image set using the *Chandra* High Energy Transmission Grating Spectrometer. These reveal bright lines from the Lyman series of C VI, O VIII, Ne X and Mg XII, and from the helium series of O VII, Ne IX, Mg XI and Si XIII, as well as faint Fe L-shell lines originating from the ISM gas swept up in the outer blast wave.

The dynamics of the oxygen-rich ejecta was studied by Tuohy & Dopita (1983) using 11 low-resolution ($R \sim 600$) long-slit spectra. Emission was detected from -2500 up to nearly +4000 km s $^{-1}$. They interpreted the emission as arising from a highly distorted ring of gas expanding roughly in the plane of the observer and estimated an expansion age ~ 1000 yr. In the X-ray, a Doppler analysis of the *Chandra* High Energy Transmission Grating Spectrometer image set by Flanagan et al. (2004) indicates velocities ~ 1000 km s $^{-1}$ and a toroidal (or possibly cylindrical) distribution of expanding gas was inferred.

Finkelstein et al. (2006) obtained second-epoch HST imaging of 1E 0102.2-7219, and were, for the first time, able to derive the proper motion of the oxygen-rich filaments. From this they were able to infer a kinematic age for the SNR of 2050 ± 600 yr - about twice that obtained by Tuohy & Dopita (1983) from the expansion velocity and the projected physical size, and also twice that derived by Hughes et al. (2000) from an analysis of *Chandra* X-ray data.

These disparate geometrical models and derived ages clearly predicate the need for a new optical study of 1E 0102.2-7219. This has been made possible by the advent of the *Wide Field Spectrograph* (WiFeS) on the 2.3m telescope operated by the Australian National University at the Siding Spring Observatory. This instrument whose design was described by Dopita et al. (2007) and whose performance was given in Dopita et al. (2010a) provides a (fully filled) field of view of 38×25 arc sec., a spatial resolution element of 1.0×0.5 arc sec, spectral resolutions of either 3000 or 7000, and a wavelength coverage of 3200-9600 Å. In this paper we describe our observations of the dynamics of the [O III] 5007Å emitting filaments, and use these to derive a complete 3-D model of the dynamics of this fascinating SNR.

2. The Observations

Spectroscopic maps of the supernova remnant 1E 0102.2-7219 (hereafter 1E0102 for brevity) were obtained at a resolution $R = 3000$ in the blue and $R = 7000$ in the red. Data were acquired in two separate observing runs on September 18, 2009 and December 11, 2009 at the Siding Spring Observatory, using WiFeS (Wide Field Spectrograph, see Dopita et al. (2007, 2010a)) on the ANU 2.3m telescope. These data consist of a mosaic of four fields chosen to encompass the remnant and the neighboring ionized ring-like region. Each field spans 25×38 arc sec. with 0.5 arc sec. sampling in the spatial direction, and 1.0 arc sec. in the spectral direction. The data were subsequently interpolated to provide 0.5×0.5 arc sec. pixels. The total field of view spans $\sim 76 \times 50$ arc sec. in RA and in declination, respectively.

Because of errors and drift in the pointing, changes in atmospheric dispersion, and an error in setting the correct position angle, the four quadrants are not perfectly aligned. Following the reduction of the data, described below, we were able to establish the pointing of each data quadrant *a posteriori* by referencing the star fields to the high-resolution HST image of the SNR. The deduced position of each quadrant and labeling of the fields is shown in Fig. 1.

The NE, SE and NW fields were obtained (in this order) during the first observing run on 18th September 2009. The seeing ranged from 1.5 arc sec. at the beginning of the night up to 2.1 arc sec. at the end. The data in the SW quadrant were obtained during the second run on 11th December 2009, in 1.5 arc sec. mean seeing conditions. The resulting spectral coverage ranges from $\lambda 3200$ Å to $\lambda 5900$ Å for the blue image, and $\lambda 5290$ Å to $\lambda 7060$ Å for the red image. Both the red and blue images are taken simultaneously, and the light from the telescope is split using the dichroic referred to as RT560 in Dopita et al. (2010a).

All images were acquired with 1×1 pixel binning using the WiFeS “Nod-and-Shuffle” data acquisition mode (see Dopita et al. 2010a). Each image consists of 10 cycles of 120 sec. on the object and 10 interleaved cycles of 60 sec. on the sky, giving a total on-object exposure of 1800 sec and a total image exposure time (including the overheads for guide-star acquisition and readout) of about 2850 sec. Three such images of each of the four fields were taken to allow for adequate cosmic ray subtraction.

3. Data reduction

3.1. Individual fields

The four fields have been reduced separately using the WiFeS reduction pipeline based upon IRAF¹ scripts. This has been described in Dopita et al. (2010a).

The same calibration files were used for the NE, SE and NW fields. These consist of a dome wire, a dome flat, two sky flats (taken at dusk), a bias and an Ne Ar arc exposure, all taken during the first observing night. Because the instrument is exceedingly stable, the same dome wire, dome flat and sky flats have been used for the SW field reduction, along with a bias frame and a Ne Ar arc exposure taken on the second observing night.

Each three images of every four fields are bias subtracted, flat fielded and sky subtracted, atmospheric dispersion corrected, and finally combined and reduced to a wavelength calibrated 3-D data cube from which the spectra of individual regions can be extracted, or from which monochromatic images of the whole field can be formed. We have not calibrated the data to absolute flux units using observations of photometric standard stars, as this was not required for the purposes of this paper.

The issue of the bias subtraction deserves a special mention. The WiFeS bias frames are subject to small temporal variations, but have little or no fixed pattern noise. Since each chip is read out in all four on-chip amplifiers, each quadrant of the bias frame may vary in intensity, and also with respect to the others, as well as suffering small changes in the slope of the mean intensity across the chip. Such variations prevent us from constructing a Master Bias using the standard median techniques. Instead, our Master Bias consists of four smooth planes (one in each quadrant), each one representing the best fit to an individual bias frame. This technique, developed by Jeffrey Rich of the University of Hawaii (private communication) shows very little variation in the bias-subtracted data depending on the time lapse between the Bias acquisition and the Science frame acquisition, and it produces reduced images of better quality when compared to other more standard techniques of bias subtraction.

¹IRAF is distributed by the National Optical Astronomy Observatory, which is operated by AURA, Inc., under cooperative agreement with the National Science Foundation.

3.2. Merging the fields into a Mosaic

The four fields were merged into a Master Cube to form the final mosaic. First order alignment of the fields simply used the information contained within the header. We then confirmed the orientation of the separate fields using the position of the three stars in the SW field found in the 2MASS database (see Skrutskie et al. 2006). Their respective 2MASS designations, sky coordinates and the final $x - y$ positions found for these stars in our image are shown in Table 1.

Simple trigonometry gives a rotation of the SW field of $\Delta\theta = 1.6 \pm 0.8$ degrees with respect to the RA direction. Amongst the three reference stars, the first one lies on the edge of the SW field, and the third one is extremely faint, which accounts for much of the error in the determination of orientation angle. Since this angle corresponds to a shift of only 1.06 pixels on the edge of the picture, given the error in its determination, we decided not to take it into account. Due to an observing error, the NW, NE and SE fields are rotated in Position Angle by 5 degrees with respect to the SW field. This has been fully taken into account. The fuzzy edges of these quadrants results from the linear interpolation used in the rotation of the image cube.

Once this initial orientation had been determined, the fine alignment of the fields was made manually by aligning the quadrants using the HST optical image of Rho et al. (2009), based on the data of Finkelstein et al. (2006). The final alignment has an accuracy of 1 pixel, or 0.5 arc sec. The (x-y) shifts deduced from the header and the second-order stellar photometric shifts used to build the Master Cube are shown respectively in the columns (2-3) and (4-5) of Table 2.

The five first and five last lines of WiFeS images display high signal variations due to vignetting and atmospheric dispersion effects. Those regions have been trimmed for each field before building the mosaic. The final mosaic thus spans ~ 70 arc sec. along the Declination direction. In the overlap regions, the pixel value is taken as the median of the overlapping pixel values.

We detected a wavelength shift for one image slice ($\cong 0.8$ Å) in the SW field. This shift is due to a poor quality of the calibration image of the Ne Ar reference arc used for this field. This was corrected manually. An absolute flux calibration was not required. However, we scaled the SW and SE fields by factors of 1.5 and 1.3, respectively, in order to match the signal intensity in the overlapping regions of the data cube.

4. Results

Our analysis is based on the dynamics of the [O III] λ 5007 Å forbidden line, which is part of the $\lambda\lambda$ 4959, 5007 Å doublet. Because of the large velocity dispersion in this SNR, in some regions the two emission lines are blended. This blending is clearly visible in Fig. 2, where we display a characteristic spectrum of the surrounding X-ray ionized medium of 1E0102, a spectrum of the SNR demonstrating blending, and a deblended spectrum derived using the procedure described below.

The wavelengths of the H β , and [O III] $\lambda\lambda$ 4959, 5007 Å lines arising from the surrounding ISM are marked in dotted lines in Fig. 2. The widths of these lines are determined by the instrumental resolution, since the local turbulence in the interstellar gas is low. Their measured wavelengths are respectively 4864.2, 4961.5 and 5009.4 Å. Comparing with their respective rest frame wavelength of 4861.3, 4958.9 and 5006.7 Å (e.g. Groves et al. 2002; Dopita & Sutherland 2003, and references therein), we deduce the heliocentric radial velocity for the interstellar gas surrounding the SNR to be 158 ± 9 km s $^{-1}$. This value is consistent with the HI radial velocities found by Staveley-Smith et al. (1997) in this area of the SMC.

An example of a spectrum demonstrating the line blending issue is shown in Fig. 2-(b). Fortunately, we can lift up the degeneracy using the known (and fixed) 4959 to 5007 Å intensity ratio of 1 to 2.86 (e.g. Dopita & Sutherland 2003). Thus, we simply scale down the spectrum by 1/2.86, blue-shift it by 48 Å and subtract it to the original spectrum. This procedure will remove all the λ 4959 contribution from the region of the spectrum $\lambda\lambda$ 4959-5007. The de-blended spectrum should not be trusted at wavelengths smaller than 4959 Å, as the method will create artifacts in these regions. Fortunately, there is no case in which the radial velocity of the ejecta exceeds -2800 km s $^{-1}$, sufficient to shift the 5007 Å emission shortward of 4959 Å. If this were the case, then the blue wing of the 4959 Å line would need to be used in the cleaning procedure, but this has lower signal to noise. The spectrum resulting from our simple cleaning method is shown in Fig. 2-(c). Clearly, it is free from the 4959 Å [O III] line contribution.

4.1. Velocity Map

In Fig. 3, we present the first complete [O III] λ 5007 Å velocity map of the oxygen-rich ejecta in 1E0102. Each slice covers a velocity distribution width of 500 km s $^{-1}$ except for the zero velocity slice which covers a total velocity range of 240 km s $^{-1}$. The mean velocity $\langle v_r \rangle$ is indicated for reference. The frames use a square root intensity stretch, in order to better reveal the fainter knots. The zero velocity reference is the systemic velocity of the

SMC found in Sect. 4.

Note the much greater intensity of the zero-velocity frame due to the diffuse ISM halo surrounding the supernova remnant (also seen in Fig. 1). This nebulosity displays strong He II $\lambda 4686$ emission, as well as a very high [O III] 4363/5007 Å ratio, and therefore is certainly X-ray ionized by the SNR. The fact that the emissivity of this nebula does not show a strong variation around the supernova remnant indicates that the surrounding ISM is fairly uniform, and therefore has had little influence in shaping the SNR blast wave.

We note a strong asymmetry in the distribution of the knots, as it was already observed in the previous studies of 1E0102 at visible wavelengths (Tuohy & Dopita 1983). The bright knots are mostly blue-shifted. They lie on broken arc structures, distributed over most of the projected area of the oxygen-rich filament structure. Less dense knots can be seen on the red-shifted side, forming broken loops as well, but with generally smaller radius. Blue-shifted knots' velocities range up to ~ -2500 km s $^{-1}$, while red-shifted ones go up to $\sim +3500$ km s $^{-1}$. The distorted ring model of Tuohy & Dopita (1983) is not able to explain the long, fainter continuous blue-shifted arcs found in this map (*c.f.* their Fig. 4). It also fails because of the smaller arc radius in the red-shifted material. The existence of the inner small bright and outer long dim arcs in the $< v_r > = 250$ km s $^{-1}$ panel present a problem to the cylindrical model, as well as to the model of a non-uniform spherical shell with azimuthal symmetry of Flanagan et al. (2004). Clearly, a more complex model is needed. In the following Section, we will show that the actual shape of the ejecta in 1E0102 can be understood as an asymmetric bipolar structure.

5. The 3-D map of the ejecta

The oxygen-rich filaments are excited as clouds of ejecta cross the reverse shock, which drives a slow shock and an ionization front into them (Sutherland & Dopita 1995). Since the slow shock is much slower (~ 100 km s $^{-1}$) than the speed at which they cross the reverse shock (~ 2000 km s $^{-1}$), we can assume that the oxygen-rich filaments have been travelling ballistically since the time of the explosion. Therefore, the space velocity, v , of O-rich knots is $v = R \cdot T^{-1}$, where R is the distance of the knot to the center of the SNR, and T is the time since the explosion.

Finkelstein et al. (2006) used HST proper motion measurements of the filaments to establish an age of $T = 2050 \pm 600$ years for 1E0102. Other age estimates obtained using radial velocity measurements (see e.g. Tuohy & Dopita 1983) were of the order of ~ 1000 years. Those estimations are based on a spherical shape assumption, which we show in the

previous Section do not fit the actual shape of the ejecta in 1E0102. It is thus clear that the proper motion age estimate provides a much more trustworthy value, as it is not biased by any assumptions about the ejecta shape. This then allows us to construct a complete 3-D map of the ejecta. Projecting along the line of sight, v becomes the radial velocity v_r , and R becomes z . Therefore the transformation of the observables to 3-D coordinates is:

$$\begin{aligned} v_r \text{ [km s}^{-1}\text{]} &\rightarrow z \text{ [pc]} = v_r \cdot T \\ x \text{ [arc sec]} &\rightarrow x \text{ [pc]} = x \text{ [arc sec]} \cdot D \text{ and} \\ y \text{ [arc sec]} &\rightarrow y \text{ [pc]} = y \text{ [arc sec]} \cdot D \end{aligned}$$

where D is the distance to the SMC, taken as 59 kpc (van den Bergh 1999). At the estimated distance and age, $\Delta v_r = 1000 \text{ km s}^{-1}$ corresponds to $\Delta z = 2.04 \text{ pc}$. Or equivalently, $\Delta z = 1 \text{ pc}$ corresponds to $\Delta v_r = 490 \text{ km s}^{-1}$.

The computed projections of the 3-D ejecta map are shown in Fig. 4. The left column shows the top view of 1E0102, as seen from the Earth. The middle column shows the projection along the Declination axis and the z -direction, while the right column gives the projection on the Right Ascension axis and the z -direction. The direction of the Earth is to the top of those two columns. Every frame uses a rainbow color table with a linear intensity stretch. The accumulated photon count for each panel is given in the caption to Fig. 4. The readout and sky noise in the image cube corresponds to about 8 photons per pixel.

In Fig. 4, the vertical strips are the spectra of the field stars. The other features are the O-rich knots. The horizontal plane in the middle and right columns corresponds to the radial velocity of the X-ray ionized interstellar gas. It is not visible in the left column, as we did not plot the gas with $-150 \text{ km s}^{-1} \leq v_r \leq 150 \text{ km s}^{-1}$, in order to avoid filling the whole surface, which would hide the structure of the O-rich knots. The extreme clumpiness of the shell is clearly seen, with individual blobs and filaments highlighted by their intensity variations, limited by the spatial resolution of the data cube imposed by seeing and by spatial sampling. At the estimated distance, the ejecta span $\sim 9 \text{ pc} \times \sim 11 \text{ pc}$.

The ejecta do not trace out a spherical shell. Looking at the lower four panels of Fig. 4, we see that the brightest filaments trace an incomplete ring of gas, which has a systematic blue-shift. The fainter blobs are associated with this, and partially fill out a conical approaching shell of gas. The faintest material fills out the red-shifted (distant) side of the shell, which is physically wider and deeper than the approaching side. The far side becomes wider at its lower extremity, and is entirely free of emitting clouds at its bottom. In brief, the structure of the shell is reminiscent of an inverted water glass, with its axis inclined at about 40 degrees to the line of sight. This strongly suggests a predominantly bipolar ejection of matter, but with a strong asymmetry.

The 3-D structure of the remnant becomes clear in the stereo images² drawn from the 3-D map, which are shown in Fig. 5 and 6. In these stereo pairs, the emission from the zero-velocity material is not plotted, as it would obscure the details of the 3-D structure of the ejecta themselves. In fact, the zero-velocity emission from the SNR is best traced in Fig. 3. Note that there is an inner ring of emission, and a region of very high emissivity close to the edge of the SW segment which may be associated with flux enhancements observed in the radio, X-ray and IR maps (Rho et al. 2009).

To complement the information in these stereo pairs, we have also constructed an interactive color 3-D map of the ejecta, shown in Fig. 7. Based on the concept described by Barnes & Fluke (2008), we have used the ability of Adobe Portable Document Format (.pdf) files to host interactive 3-D objects. We have used Python and MayaVi in order to generate a CAD-like³ 3-D map of the ejecta of 1E0102, and *Adobe Acrobat 9 Pro extended* to produce a .pdf of it. This .pdf, with a size of ~ 10.5 Mo, is freely available for download here : <http://www.mso.anu.edu.au/~fvogt/1e0102.html>. In order to be viewed, the only software needed is an up-to-date version (v.8 or above) of Adobe Acrobat Reader⁴. The user is able to interact in several ways with the resulting file : rotate around the ejecta, or zoom in and out at will, for example. A handy cross-section tool is also available.

The data and the color code used in this 3-D map are identical to the top row of Fig. 4. It represents the low intensity ejecta, with the number of counts per pixel ranging from 15 - 60. Note that the low velocity gas, with $-150 \text{ km s}^{-1} \leq v_r \leq 150 \text{ km s}^{-1}$ is not plotted in order to avoid filling the map, and obscuring the high-velocity details. Each pixel is represented by a circle (and not a sphere) of fixed radius in order to keep the size of the file as small as possible. As a result, the ejecta are slightly transparent in this representation. In the *Model Render Mode* options list, the user can select *Shaded Vertices* which will give a non-transparent aspect to the ejecta. We find this visualization mode especially interesting when used together with the Cross Section tool mentioned previously. Three red-green-blue axes, located on the bottom left of the map, enable to orientate the map in the 3-D space. The red-X axis corresponds to the Dec direction, while the green-Y axis corresponds to the RA direction, and the blue-Z axis corresponds to the line of sight, with the Earth in the

²Stereo pairs or stereograms enable us to see a Real 3-D image of an object using two 2-D images. The two projections are separated by 5 degrees in azimuth. By crossing ones eyes, we can reconstruct the 3-D image of the object in between the two projections. See <http://spdbv.vital-it.ch/TheMolecularLevel/0Help/StereoView.html#con> for a detailed tutorial and training examples of this visualization technique, which is widely used in Biochemistry.

³CAD=Computer-Aided Design

⁴<http://get.adobe.com/reader/>

positive direction.

Finally, we have also created a Real 3-D movie of our 3-D map. This movie can be played in 3-D theaters with the suitable equipment and configuration. But our main intention is for it to be looked at using the stereo pairs viewing technique described above. The movie, in an .mpg format, can be freely downloaded here : <http://www.mso.anu.edu.au/~fvogt/1e0102.html>. We are preparing a paper in which we will discuss those stereo pairs techniques into more details, describe how they can be easily produced, and illustrate the technique with different astrophysical applications using observational and theoretical examples (see Vogt et al. 2010).

6. Discussion

The asymmetry of the ejecta in 1E0102 has two possible causes and three possible scenarios, each of which has been mapped out in the introduction: it can be caused by an intrinsic asymmetry in the interstellar/circumstellar environment, an intrinsic asymmetry during the fireball stage of the SN explosion, or a mix of the two. In projection, 1E0102 lies close to the HII region N76 in the catalog of Davies et al. (1976). Whether they are indeed associated remains uncertain. Pakull & Bianchi (1991) and Finkelstein et al. (2006) suggested the existence of a possible association in between the two. If those objects are indeed interacting, one would expect the ISM density to decrease from the SW to the NE, away from N76. The ring of ionized gas surrounding the SNR is a good mean to probe the intensity of the medium surrounding 1E0102. As it can be seen in Fig. 1, its intensity slightly *increases* along the SW-NE direction. This indicates a possible increase of the ISM density *away* from N76. An interaction of N76 with 1E0102 thus seems rather unlikely. It is also unlikely that a density gradient in this local ISM could be the cause of the strong asymmetry seen in the distribution of ejecta. The ejecta are distributed about an axis inclined at $\sim 40^\circ$ with respect to the line of sight, along a NNW-SSE orientation with blue-shifted material towards the SSE, but the possible ISM density gradient, as suggested by the ISM emission, lies along a direction almost perpendicular to this (SW-NE).

The relationship between the shape of the reverse-shock surface through which the oxygen-rich knots are passing, and the intrinsic shape of the initial explosion fireball is rather complex. In projection, 1E0102 as seen at X-ray wavelengths seems to form the classical spherical blast-wave / reverse shock structure. However, the radial velocities observed in the X-ray lines already indicated a toroidal (or possibly cylindrical) distribution of expanding gas showing that the shape of the explosion is certainly not spherical (Flanagan et al. 2004).

In the classical model, the reverse shock first tracks the blast wave, and then as increasing amounts of ISM or circum-stellar material are swept up, it slows down, and finally reverses direction until all of the ejecta have been thermalized. 1E0102 is seen relatively early in this sequence; the reverse shock has a radius about 68% of the blast wave radius (Rho et al. 2009). Therefore, asymmetry in the shape of the reverse shock has to arise from azimuthal differences in the velocity of the fastest-moving ejecta and, to some extent, differences in the kinetic energy density of the ejecta. Hence, it seems reasonable to conclude that the asymmetry seen in the ejecta of 1E0102 is mostly due to an explosion with a preferred axis which is presumably imposed by rotation of the progenitor star, accompanied with a strong asymmetry between the two lobes of the explosion. Such a scenario has also been suggested for the cases of Cas A and Puppis A (see the discussion in Sec. 1).

Our 3-D map of the ejecta in 1E0102 will be particularly useful in helping to guide simulations of core-collapse supernovae. Recently, these simulations have made great progress at the level of the physics they include, the number of spatial dimensions, their spatial resolution and the time interval they can span. Despite this progress, the physics of the secular instabilities and the details of the explosion mechanism remains uncertain.

All agree that the explosion energy is provided by the neutrinos created during the creation of the proto-neutron star (PNS) (see e.g. Woosley & Janka 2005), but with 1-D or 2-D simulations, an explosion could not be produced. Recently, these simulations entered the 3-D world (Fryer & Warren 2002) and the need for, and importance of, asymmetries in the SN explosion mechanism became more and more evident. Preliminary results suggest that both rotation and magnetic field can play an important role in the process. Several mechanisms, involving these singly or in combination have been suggested, such as the neutrino bubble instability of Socrates et al. (2005). Due to the complexity of the problem however, no current code can provide a complete picture of the initial explosion. When the interaction of the ejecta with the outer layers of the star, or with the circum-stellar environment is also considered, the picture gets even more complex. Simulations have been continued to as much as a year or so after the explosion (see e.g. Hungerford et al. 2005), but in the majority of evolved SNR, the ejecta have been altered by their encounter of the circumstellar and/or interstellar material, preventing any direct comparison between simulations and observations.

Our 3-D map of 1E0102, by providing an image of the shape and distribution of the inner ejecta of the supernova event, provides an interesting test bed and comparison point for any simulated SN explosions - eliminating projection effects which might otherwise confuse the comparison of observations and simulations. The ejecta in 1E0102 strongly suggest strong asymmetries are present during the explosion mechanism itself, both in the distribution of the ejecta and in their space velocities. We do not find a clear double jet structure, such as

simulated by Khokhlov et al. (1999), for example. However we note a striking resemblance to some of the single-lobe explosion models of Hungerford et al. (2005), especially in the degree of the observed asymmetry, suggesting that such models may be appropriate to our object.

7. Summary

We have obtained a 3-D spectroscopic map in the [O III] $\lambda 5007 \text{ \AA}$ forbidden line of the SNR 1E0102 in the SMC, using the Wide Field Spectrograph on the 2.3m telescope of the Australian National University at Siding Spring Observatory. Our data show:

- Most of the ejecta are blue-shifted, with radial velocity as high as -2500 km s^{-1} while the less luminous material, with smaller filling factor reaches radial velocities as high as $+3500 \text{ km s}^{-1}$.
- The global shape of the reverse shock, as traced by the oxygen-rich material has a preferred axis inclined $\sim 40^\circ$ with the line of sight, and lies along a NNW-SSE direction. The ejecta span a region $\sim 9 \text{ pc} \times \sim 11 \text{ pc}$, display a pronounced bilateral asymmetry about the preferred axis and have two pronounced rings of filaments at each end. They form a shape reminiscent of an inverted and inclined water glass.
- From the shape and orientation of the ionized emission ring surrounding 1E0102, we deduce that the strong asymmetries displayed by the ejecta are most certainly mostly due to asymmetries within the SN explosion, and not to some density gradient within the surrounding medium.

Our reconstructed 3-D map represent a rare view of the young, almost unaltered result of a core-collapse SN explosion. This 3-D map of O-rich ejecta thus constitutes a direct test for core-collapse simulations, which certainly is the first of its kind. Our map of the ejecta is consistent with the growing consensus that asymmetry plays a key role in the SN explosion, whether it is caused by convective, magnetic, and/or rotational instabilities. Finally, we have recently obtained similar data for another oxygen-rich core-collapse supernova remnant, N132D in the LMC, for which we plan a similar analysis.

We thank the anonymous referee for his constructive review that helped us improve the presentation of the data in this article. Dopita acknowledges the support of the Australian Research Council (ARC) through Discovery projects DP0984657 and DP0664434. This research has made use of data products from the Two Micron All Sky Survey, which is a

joint project of the University of Massachusetts and the Infrared Processing and Analysis Center/California Institute of Technology, funded by the National Aeronautics and Space Administration and the National Science Foundation. It has also used the NASA/IPAC Extragalactic Database (NED) which is operated by the Jet Propulsion Laboratory, California Institute of Technology, under contract with the National Aeronautics and Space Administration. This research has also made use of NASA's Astrophysics Data System, and SAOImage DS9, developed by the Smithsonian Astrophysical Observatory.

REFERENCES

- Amy, S. W. & Ball, L. 1993, ApJ, 411, 761
- Barnes, D. G. & Fluke, C. J. 2008, New Astronomy, 13, 599
- Blair, W. P., Morse, J. A., Raymond, J. C., et al. 2000, ApJ, 537, 667
- Chevalier, R. A. & Kirshner, R. P. 1978, ApJ, 219, 931
- Danziger, I. J. & Dennefeld, M. 1976, ApJ, 207, 394
- Davies, R. D., Elliott, K. H., & Meaburn, J. 1976, MmRAS, 81, 89
- Dopita, M., Hart, J., McGregor, P., et al. 2007, Ap&SS, 310, 255
- Dopita, M., Rhee, J., Farage, C., et al. 2010a, ArXiv e-prints
- Dopita, M. A., Binette, L., & Tuohy, I. R. 1984, ApJ, 282, 142
- Dopita, M. A., Blair, W. P., Long, K. S., et al. 2010b, ApJ, 710, 964
- Dopita, M. A. & Sutherland, R. S. 2003, *Astronomy & Astrophysics Library*, Springer-Verlag: Berlin, Heidelberg, NY
- Dopita, M. A. & Tuohy, I. R. 1984, ApJ, 282, 135
- Dopita, M. A., Tuohy, I. R., & Mathewson, D. S. 1981, ApJ, 248, L105
- Fesen, R. A., Hammell, M. C., Morse, J., et al. 2006a, ApJ, 636, 859
- Fesen, R. A., Hammell, M. C., Morse, J., et al. 2006b, ApJ, 645, 283
- Fesen, R. A., Morse, J. A., Chevalier, R. A., et al. 2001, AJ, 122, 2644
- Finkelstein, S. L., Morse, J. A., Green, J. C., et al. 2006, ApJ, 641, 919

- Flanagan, K. A., Canizares, C. R., Dewey, D., et al. 2004, ApJ, 605, 230
- Fryer, C. L. & Warren, M. S. 2002, ApJ, 574, L65
- Gaetz, T. J., Butt, Y. M., Edgar, R. J., et al. 2000, ApJ, 534, L47
- Goss, W. M., Shaver, P. A., Zealey, W. J., Murdin, P., & Clark, D. H. 1979, MNRAS, 188, 357
- Groves, B., Dopita, M. A., Williams, R. E., & Hua, C. 2002, Publications of the Astronomical Society of Australia, 19, 425
- Hines, D. C., Rieke, G. H., Gordon, K. D., et al. 2004, ApJS, 154, 290
- Hughes, J. P., Rakowski, C. E., & Decourchelle, A. 2000, ApJ, 543, L61
- Hungerford, A. L., Fryer, C. L., & Rockefeller, G. 2005, ApJ, 635, 487
- Hwang, U., Laming, J. M., Badenes, C., et al. 2004, ApJ, 615, L117
- Itoh, H. 1981, PASJ, 33, 521
- Khokhlov, A. M., Höflich, P. A., Oran, E. S., et al. 1999, ApJ, 524, L107
- Kirshner, R. P. & Blair, W. P. 1980, ApJ, 236, 135
- Kirshner, R. P. & Chevalier, R. A. 1977, ApJ, 218, 142
- Laming, J. M., Hwang, U., Radics, B., Lekli, G., & Takács, E. 2006, ApJ, 644, 260
- Lasker, B. M. & Golimowski, D. A. 1991, ApJ, 371, 568
- Lee, J., Park, S., Hughes, J. P., et al. 2010, ApJ, 711, 861
- Mathewson, D. S., Dopita, M. A., Tuohy, I. R., & Ford, V. L. 1980, ApJ, 242, L73
- Murdin, P. & Clark, D. H. 1979, MNRAS, 189, 501
- Pakull, M. W. & Bianchi, L. 1991, in IAU Symposium, Vol. 143, Wolf-Rayet Stars and Interrelations with Other Massive Stars in Galaxies, ed. K. A. van der Hucht & B. Hidayat, 260
- Rasmussen, A. P., Behar, E., Kahn, S. M., den Herder, J. W., & van der Heyden, K. 2001, A&A, 365, L231
- Rho, J., Reach, W. T., Tappe, A., et al. 2009, ApJ, 700, 579

- Sasaki, M., Stadlbauer, T. F. X., Haberl, F., Filipović, M. D., & Bennie, P. J. 2001, A&A, 365, L237
- Schure, K. M., Vink, J., García-Segura, G., & Achterberg, A. 2008, ApJ, 686, 399
- Seward, F. D. & Mitchell, M. 1981, ApJ, 243, 736
- Skrutskie, M. F., Cutri, R. M., Stiening, R., et al. 2006, AJ, 131, 1163
- Socrates, A., Blaes, O., Hungerford, A., & Fryer, C. L. 2005, ApJ, 632, 531
- Staveley-Smith, L., Sault, R. J., Hatzidimitriou, D., Kesteven, M. J., & McConnell, D. 1997, MNRAS, 289, 225
- Sutherland, R. S. & Dopita, M. A. 1995, ApJ, 439, 381
- Tuohy, I. R. & Dopita, M. A. 1983, ApJ, 268, L11
- van den Bergh, S. 1999, in IAU Symposium, Vol. 190, New Views of the Magellanic Clouds, ed. Y.-H. Chu, N. Suntzeff, J. Hesser, & D. Bohlender, 569
- van den Bergh, S. & Dodd, W. W. 1970, ApJ, 162, 485
- van Veelen, B., Langer, N., Vink, J., García-Segura, G., & van Marle, A. J. 2009, A&A, 503, 495
- Vink, J. 2004, Nuclear Physics B Proceedings Supplements, 132, 21
- Vogt, F., Wagner, A. Y., & Dopita, M. A. 2010, Astrophysics and Space Science, in preparation
- Winkler, P. F. & Kirshner, R. P. 1985, ApJ, 299, 981
- Winkler, P. F. & Petre, R. 2007, ApJ, 670, 635
- Woosley, S. & Janka, T. 2005, Nature Physics, 1, 147

Table 1: 2MASS reference stars located in the SW quadrant used for calibrating the quadrants orientation.

Designation ^a	Dec [d:m:s] ^a	RA [h:m:s] ^a	x ^b	y ^b
01040121-7201574	01:04:01.215	-72:01:57.47	62.95	49.00
01035694-720266	01:03:56.948	-72:02:06.70	26.22	31.25
01035583-7202001	01:03:55.837	-72:02:00.19	15.26	43.97

^aSource: 2MASS catalogue (Skrutskie et al. 2006).

^bMeasured stellar coordinates in pixels

Table 2: Theoretical and applied shifts used to merge the four fields data cubes into the Master Cube.

Quadrant	Th. shift [pixels]		App. shift [pixels]	
	x	y	x	y
SW	9	0	10	0
NW	45	0	53	1
SE	0	72	0	69
NE	45	72	45	69

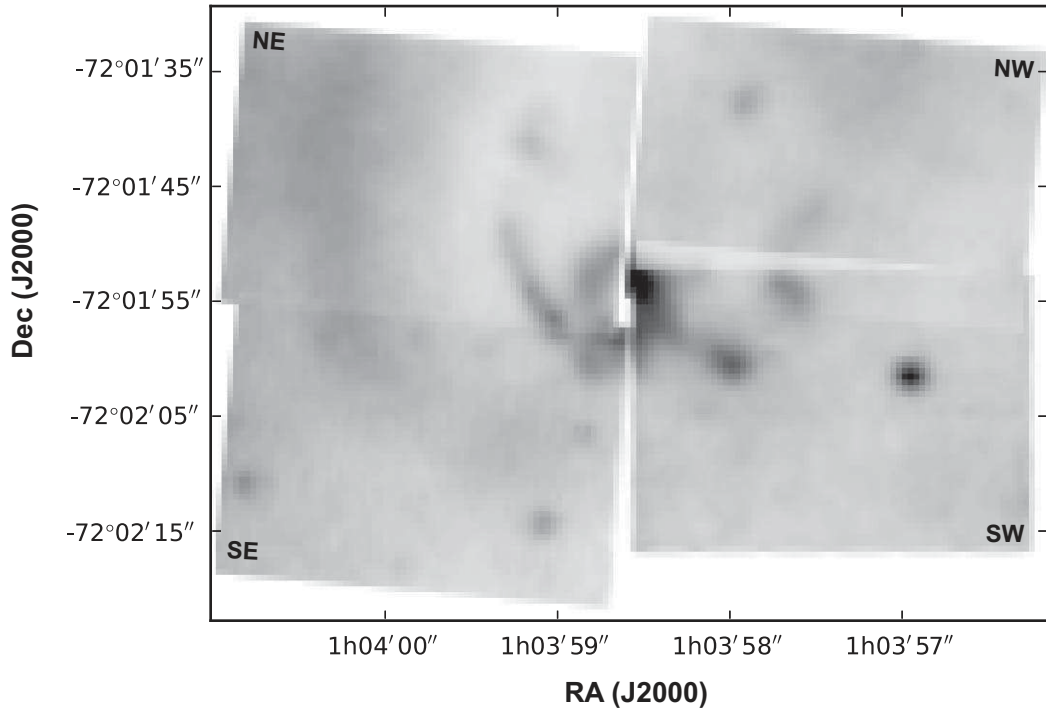


Fig. 1.— The position and orientation and labeling of the four fields observed in 1E 0102.2-7219. The images are of the gas in the velocity range -120 to $+120$ km s^{-1} . The X-ray photo-ionized halo around the SNR is clearly seen in this image of the [O III] $\lambda 5007$ forbidden line (*see* Sec. 4.1).

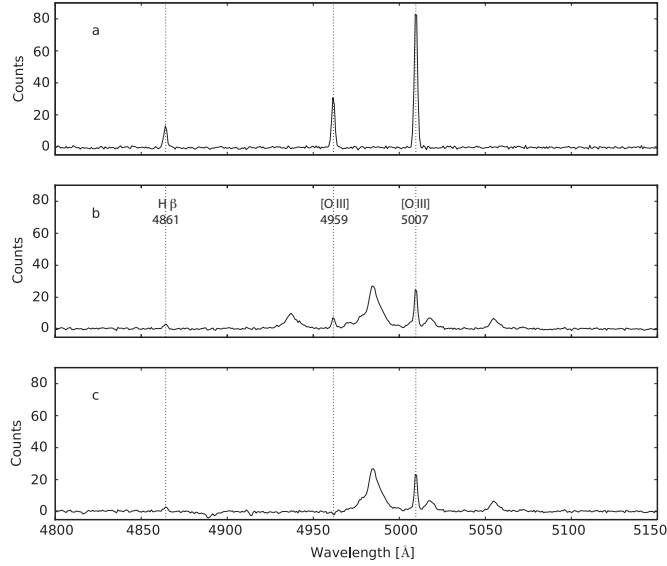


Fig. 2.— (a) A typical spectrum of region of the ISM surrounding the SNR, showing the narrow $H\beta$ and $[O\text{ III}] \lambda\lambda 4959, 5007 \text{ \AA}$ emission. These sharp lines are shifted with respect to the rest frame wavelength, due to the radial velocity of the SMC. (b) A typical spectrum of a region containing O-rich knots. The blue- and red-shifted lines are clearly visible, as well as the blending occurring in their overlap region. In panel (c) we present the same spectrum with the contribution of the $[O\text{ III}] \lambda 4959 \text{ \AA}$ line removed using the procedure described in the text. This provides the line profile used in the kinematical analysis.

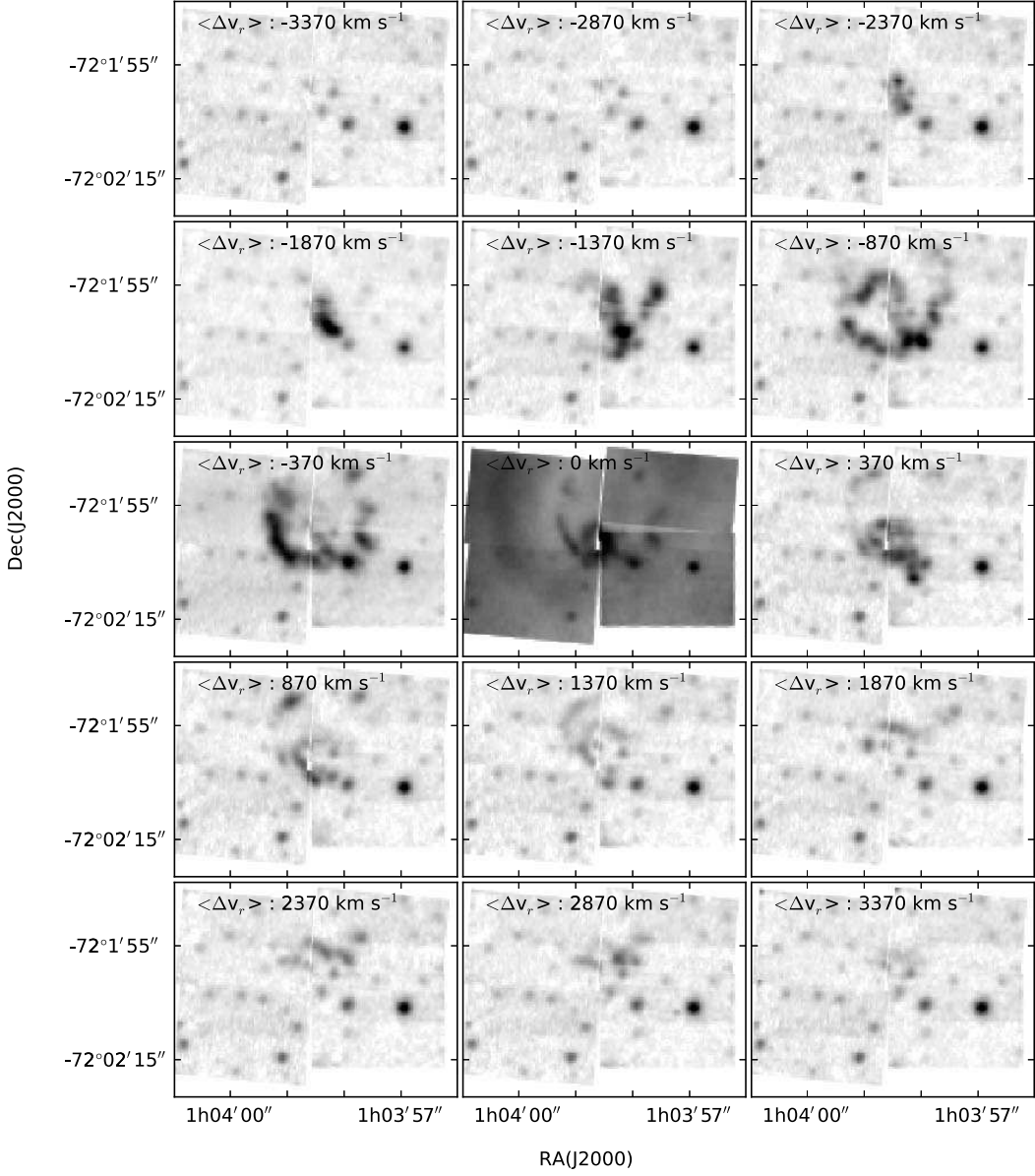


Fig. 3.— The velocity map of oxygen-rich knots, based on the [O III] $\lambda 5007$ line. The radial velocity range covered in each panel is $\Delta v_r = 500 \text{ km s}^{-1}$, except for the zero velocity channel which covers $\Delta v_r = 240 \text{ km s}^{-1}$. The mean radial velocity is indicated in each panel for reference. The image density is proportional to the squared of the normalized number of counts to bring out fainter nebulous features.

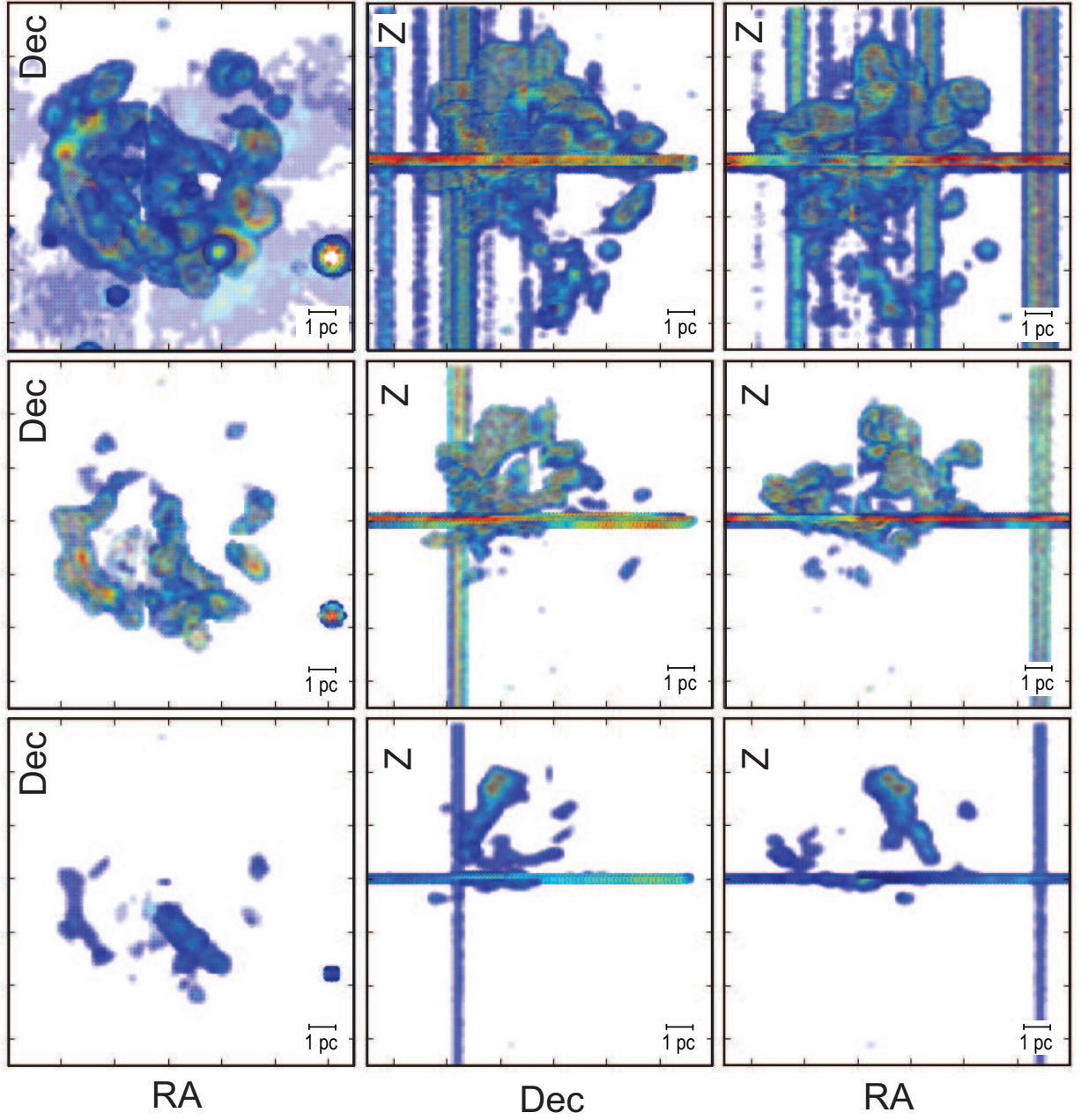


Fig. 4.— Three projections of the data cube along the X-Y, Z-X and Z-Y planes. The rainbow color ramp is linear in the number of counts per pixel, and ranges from 15 - 60 for the top trio, 60 - 120 in the middle trio, and > 120 for the bottom trio. The direction of the observer is towards the top of the page for the middle and right columns. The linear scale is given in each panel, assuming a distance to the SMC of 59 kpc (van den Bergh 1999). Each tick corresponds to 2 pc, and at the estimated distance and age, $\Delta z=1$ pc corresponds to $\Delta v_r=490$ km s $^{-1}$.

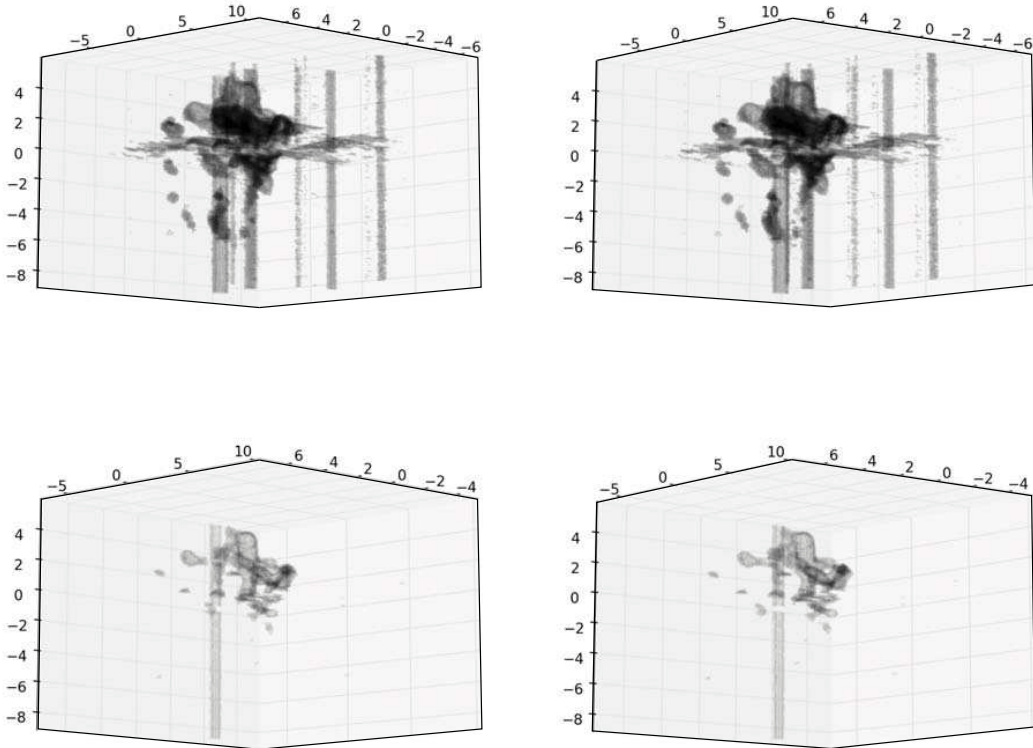


Fig. 5.— 3D stereoscopic maps of the oxygen rich ejecta in 1E0102, viewed from the NE and -10° elevation with respect to the plane of the sky. The upper pair show the weakly emitting filaments in the accumulated signal range of 15 – 60 counts per pixel, while the lower pair show the more intense features; 60 – 120 counts per pixel. The scales are given in pc, assuming a distance to the SMC of 59 kpc. At the estimated distance and age, $\Delta z=1$ pc corresponds to $\Delta v_r=490 \text{ km s}^{-1}$.

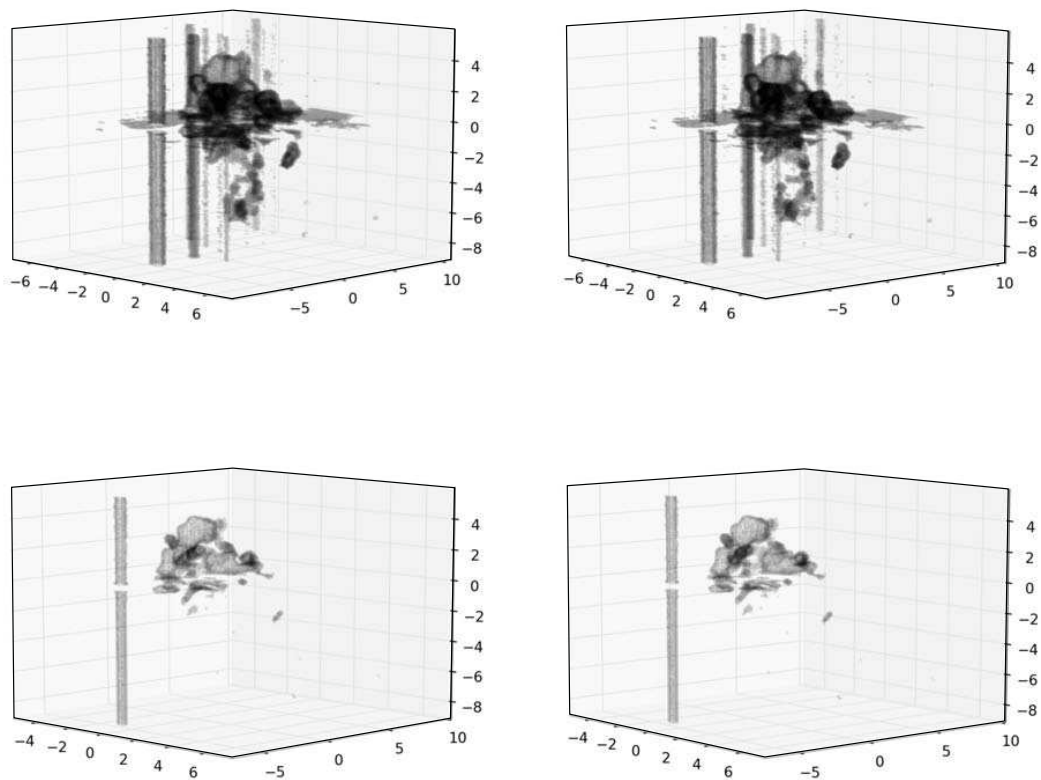


Fig. 6.— As fig. 5, but this time viewed from the NW and $+10^\circ$ elevation with respect to the plane of the sky.

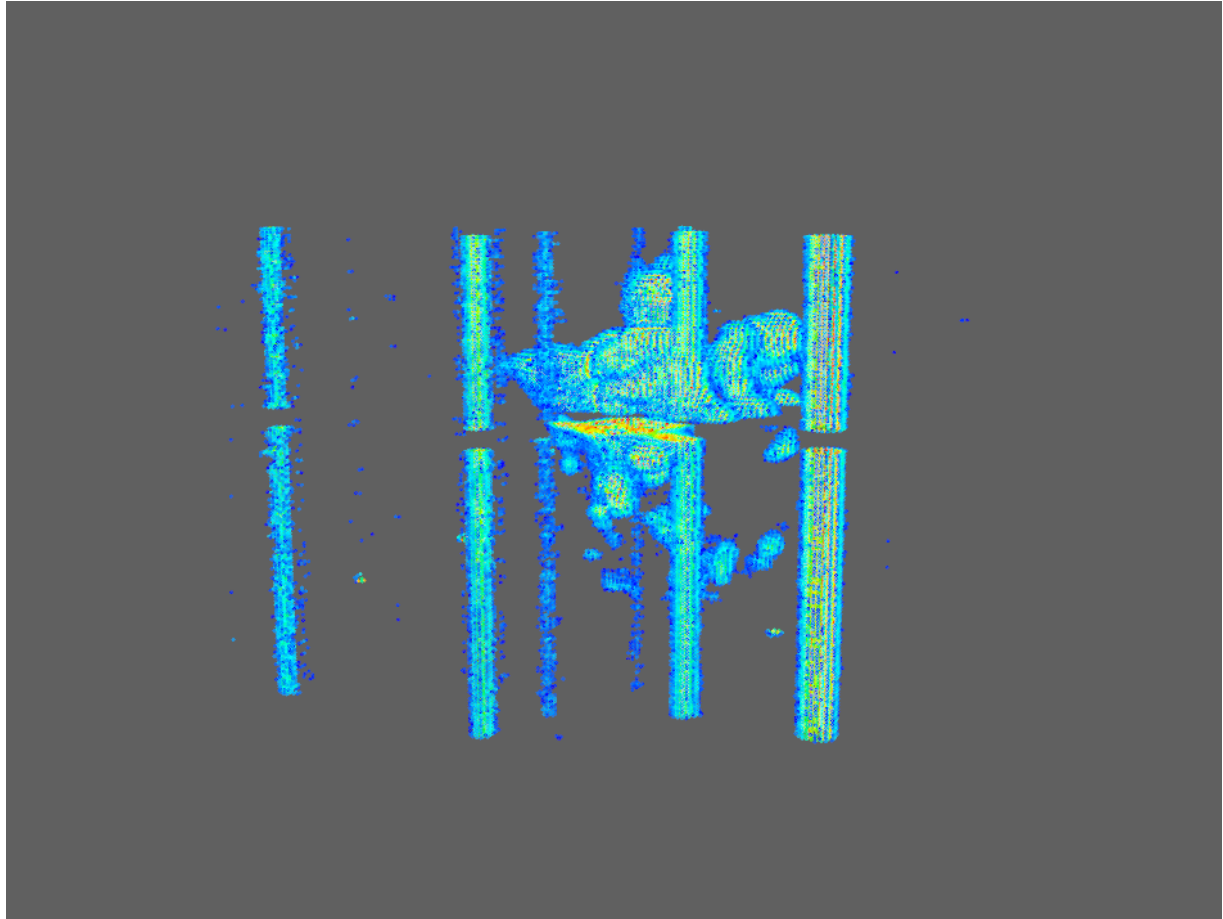


Fig. 7.— Interactive 3-D map of the ejecta in 1E0102. The data shown and the color code used are identical to the Fig. 4 top row. This map represents the low intensity ejecta, with the number of counts per pixel ranging from 15 - 60.